A cohesive interface crack model for the matrix–textile debonding in FRCM composites

Francesca Giulia Carozzi, Pierluigi Colombi *, Giulia Fava, Carlo Poggi

Department of Architecture, Built Environment and Construction Engineering (ABC), Politecnico di Milano, P.zza L. da Vinci, 32, 20133 Milan, Italy

Existing masonry structures often need to be strengthened or repaired. Among non-traditional retrofitting techniques, Fibre Reinforced Cementitious Matrix (FRCM) materials are becoming more and more interesting, especially for the reinforcement of historical buildings. The bond strength of the FRCM rein-forcement is one of the key factors affecting the behaviour of the reinforced member and failure mode mostly involves the failure of the textile/mortar interface. Based on experimental results on single lap pull–push shear tests on FRCM materials bonded to masonry blocks, a tri-linear bond–displacement behaviour at the textile–mortar interface is proposed. The last phase of the bond–slip law is characterized by a constant shear stress in order to model the friction phenomena between the matrix and the textile observed in the experimental tests. Analytical expressions for the load–displacement response and inter-facial shear stress distribution at different loading stages are derived taking into account the effects of the friction phenomena. The model is discussed in detail and the analytical results are compared to experimental outcomes. Finally, a parametric analysis is performed to highlight the effect of bond length, cohe-sive bond–slip law parameters and friction on the load–displacement response.

Keywords:
FRCM materials
Masonry
Pull–push test
Textile/mortar interface
Bond–displacement relationship
Bond strength

1. Introduction

Fibre Reinforced Cementitious Matrix (FRCM) materials represent a particular type of retrofitting technique for both concrete and masonry structures. When FRCM materials are applied, dry-fibres in textile form are impregnated with a cementitious mortar enriched with short fibres. The multifilament yarns are usually disposed in fabrics and made of alkali-resistant AR glass, carbon or polymer fibres. The matrix is typically a grout system based on cement or lime and a low dosage of dry organic polymers (less than 5% by weight). The organic compounds are necessary to ensure proper workability, setting time and mechanical properties [1].

FRCM materials present many advantages, such as lightweight, speed of execution, good mechanical properties and performance at failure. Such reinforcement type is mainly advantageous since the use of an inorganic matrix instead of an organic one allows overcoming several drawbacks of continuous fibre-reinforced materials with polymeric matrix (FRP). FRCM composites are particularly indicated in the reinforcement of historical masonry buildings, due to the higher compatibility with the substrates, vapour permeability, durability to external agents and major reversibility of the intervention [1–3]. In fact, the organic matrices penetrate into the substrate while the inorganic matrices cannot cause any damage. An overview of the use of FRCM in concrete and masonry structures can be found in [4–8].

1.1. Problem statement

FRCM reinforcement systems applied on masonry substrates present different possible failure modes. While the typical failure mode for FRP strengthening systems is debonding of a reinforcing layer with the partial detachment of the substrate [9], for FRCM materials [10–12] the common failure is observed at the mortar–textile interface and is due to slippage of the textile with respect to the mortar layer, slippage and failure of the filaments in the yarns or splitting of one layer of mortar [10–12]. Besides, the fail-ure in FRCM systems is more “ductile” due to friction and slippage phenomena occurring between the filaments in the yarn and between the yarn and the matrix. In the analysis of the bond behaviour for FRCM systems, the mechanical properties of mortar and textile are extremely important, as the impregnation between the two components characterizes the interfacial bond properties. For this reason, the textile geometry, the fibres surface chemical properties and the mortar granulometry should also be analysed in the evaluation of the bond properties. Finally, while FRP materi-

---

* Corresponding author. Tel.: +39 0223994280.
E-mail address: pierluigi.colombi@polimi.it (P. Colombi).

Published Journal Article available at: http://dx.doi.org/10.1016/j.compstruct.2016.02.019

Nomenclature

d	length of the debonded part
k_1	slope of the ascending branch in the tri-linear shear stress–displacement curve
k_2	slope of the descending branch in the tri-linear shear stress–displacement curve
l	length of the softening part
n_{yarns}	number of yarns in the fabric
p	wet perimeter of the yarn
u	yarn displacement
$\bar{u}_A$	experimental value of the displacement at the elastic limit
A	effective area of the yarn
E	Young's modulus of the yarn
K_e	elastic stiffness
F	applied force ($N(0)$)
$\bar{F}_A$	experimental value of the load at the elastic limit
$\bar{F}_B$	experimental value of the load at the end of the elastic-softening phase
L	bond length
$L_{eff,e}$	elastic effective bond length
$L_{eff,es}$	elastic-softening effective bond length
L_{opt}	optimal bond length
N	axial force of the yarn
τ	shear stress at the matrix–textile interface
τ_0	friction shear stress
τ_{max}	peak shear stress
Δ	yarn displacement at the loaded end ($u(0)$)

als are extremely thin and constant stresses may be assumed along the thickness, the FRCM systems are composed of two mortar layers with a total thickness of about 10 mm. Thus, the stresses on the external surface and on the interface between mortar and substrate could be different in comparison to the matrix–textile interface one. Due to the differences between FRP and FRCM reinforcement systems, the analytical models developed in the last years for the bond behaviour of FRP materials couldn't be applied to FRCM systems. The development of an appropriate analytical model for the evaluation of bond strength when using FRCM materials is then a need, as up to now, no analytical solution capable to predict the entire matrix–textile debonding process has been presented.

1.2. Scope of the research

First, single lap shear tests were performed on a FRCM system composed of a PBO textile embedded in a cementitious matrix applied on masonry substrates. Then, a cohesive interface crack model for the matrix–textile debonding in FRCM materials is proposed. The model allows computing the load–displacement behaviour of a FRCM material applied on masonry substrates and subjected to tangential shear forces. The shear stress–displacement behaviour at the interface was modelled by means of a tri-linear law. The last phase of the bond–slip law is characterized by a constant shear stress in order to account for the friction phenomena between the matrix and the textile observed in the experimental tests. The model parameters are calibrated from experimental results and then used in the load–slip relationship. The model is discussed in detail and is used for computing the load–displacement curves. The analytical results are compared with the experimental outcomes in terms of load–displacement curve. Finally, a parametric analysis was performed in order to highlight the influence of the bond length, the effects of the slope of the decreasing branch in the shear stress–displacement law and of the friction parameter in the load–displacement curve.

1.3. Previous studies

The bond strength of FRCM materials is very important from the design point of view and involves the definition of a specific analytical model and experimental procedures in order to calibrate the relevant coefficients [13]. In the literature the influence of different parameters was investigated, in particular the substrate mechanical properties, geometry and surface treatment, and the reinforcement mechanical properties, thickness and installation procedure.

The bond length largely influences the failure mode and the maximum load reached before the collapse of the reinforcement. The effective bond length is the minimum length needed to develop the full bond strength capacity at the reinforcement–sub-strate interface. Different analytical models and codes were proposed to define the effective bond length for FRP materials [14–16]. The main parameters that influence the computation are the elastic modulus of the reinforcement and the mechanical proper-ties of the substrate.

The fracture energy concept is generally introduced to evaluate the debonding load [17–22]. Debonding strength is usually considered to be a function of the substrate strength, width and surface treatment and of the reinforcement stiffness, width and bond length. On the other hand, all the fracture mechanics based models require the use of proper semi-empirical coefficients. These coefficients have to be evaluated on the basis of a statistical relevant number of consistent bond-shear tests.

Fracture mechanics theory allows to describe the crack formation process and to define the corresponding shear and slip distribution in all stages of the debonding process. Several analytical models based on different shear stress–slip curves were developed [14,17]. The post-peak behaviour is extremely important because when the maximum load is reached, the maximum load transfer is possible due to the interlocking or slippage phenomena. The simplest shear stress–slip curve involves a linear relationship in which no post peak behaviour is present. The typical bilinear function firstly presents a linear branch increasing up to the maximum shear stress, and then a decreasing branch where the stress linearly reduces up to the maximum strain. This shape is the most common because it fits well with the experimental data [19,23].

The analytical model proposed in this paper is specifically studied for the bond behaviour evaluation of FRCM materials. An appropriate tri-linear shear stress–slip curve is considered and the interface between matrix and textile is taken into account. The basic assumptions of the present analytical model are based on [24–26].

In [24] the bond behaviour of a FRP material applied on concrete substrate was evaluated and an analytical solution based on a bi-linear load–slip model was presented. The debonding process was discussed in detail and the prediction of the entire debonding propagation process was investigated.

To better understand the failure mechanism of cementitious composites reinforced with continuous yarns, the interaction between yarn and matrix was studied in [25]. The pull-out behaviour between a single yarn and its surrounding matrix was considered by using an analytical model based on fracture mechanics concepts. The shear failure occurring between the yarn

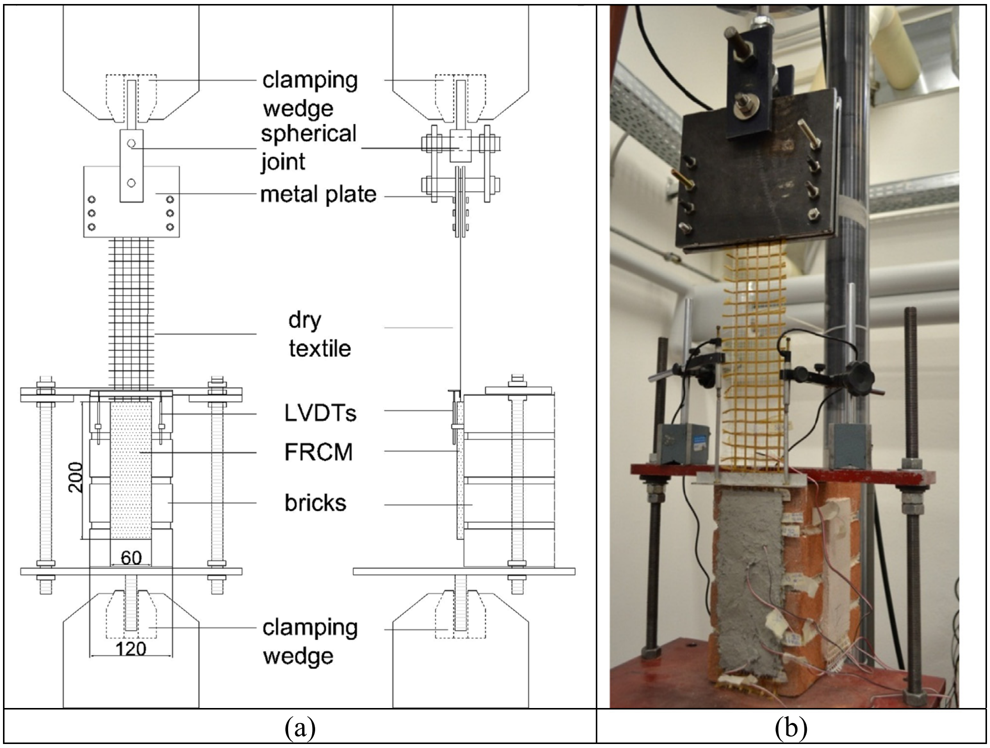

(a) (b)

Fig. 1. Test set-up: (a) pull–push testing scheme and (b) testing machine.

and the matrix was regarded as the creation of a tunnel crack at the corresponding interface. A numerical simulation was also performed. Finally, it was observed that the numerical and experimental results were in good agreement with those obtained according to the analytical model. In [26], the pull-out behaviours of a multi-filament yarn embedded in inorganic matrix was studied with a more accurate analytical model based on a fracture mechanics approach. In fact, due to the complexity of the impregnation of the multi-filament yarn into the cementitious matrix, the model also depends upon the embedded length of the yarn in the matrix. The analytical results were compared with the experimental ones.

2. Experimental evidence

An experimental campaign was performed to study the bond behaviour of FRCM reinforcement systems applied on masonry substrates. The experimental set-up is shown in Fig. 1a. Tests were performed using a testing machine with a load bearing capacity of 250 kN (see Fig. 1b). A supporting frame consisting of two threaded tie-rods and a horizontal bar was used to correctly position the specimen in the testing rig and to avoid possible misalignments of the applied load. Steel plates were used (see Fig. 1a) to connect the reinforcing grid to the testing machine. Attention was given to the alignment of the FRCM reinforcement in the specimen with the applied force. In fact, when the force is not perfectly aligned, a flexural moment may generate peeling stresses leading to premature reinforcement failure.

The FRCM material investigated is composed of a cementitious matrix and a fabric in PBO (polyparaphenylene benzobisoxazole) fibres. The mechanical properties of the textile and matrix were tested [27]. The single dry yarn has an average tensile strength of 3175 MPa and an elastic modulus of 216 GPa. The mortar has a tensile strength of 4.75 MPa, a compressive strength greater than 15 MPa and an elastic modulus greater than 6 MPa. The PBO fibre balanced fabric is made of 12 mm spaced yarns. The equivalent dry yarn area is equal to 0.221 mm^2.

The typical failure modes show the slippage (see Fig. 2a) or the tensile failure of the yarns (Fig. 2b). In some cases, mixed mode is observed with slippage and subsequent tensile failure of the yarns. Besides, the failure occurs in the reinforcement at the textile-interface or yarn level, and the substrate or the reinforcement–substrate interface is not involved in the failure mode. The mechanical properties of the textile–mortar interface play then a very important role for the FRCM reinforcement. These failure modes are different from the one observed for FRP materials where failure generally occurs in the substrate and it is due to reinforcement debonding with the detachment of a thin layer of substrate.

Slippage could appear also between the filaments in the yarn due to a telescopic failure mode. It is known that a cement matrix is not ideal to impregnate filaments. The external filaments in a yarn are in direct contact with the matrix and tightly bonded, while the internal filaments in the core of the yarn are not in direct contact with matrix and can slip more easily because of the lower friction among the fibres. An effective area of the yarn should be then defined as a fraction of the corresponding dry area. In [28–30], a model for simulating the yarn as a cylindrical structure com-prised of concentric rings, each one composed of several filaments, was presented (Fig. 3).

The yarn failure mechanism starts with the failure of the outer filament ring, followed by that of each adjacent layer until reaching the core filaments at the ultimate collapse. This pull-out telescopic mode is influenced by the matrix penetrability, the textile geometry and structure, the presence of a coating and the friction between the fibres in each yarn [31,32]. In [33], it was showed that the optimal embedded length is a decreasing function of the impregnation index. This is directly connected to the mortar penetration inside the yarn. The efficiency grows as the impregnation index increases, which is linked to the increase of the sleeve filaments due to the penetration of the matrix in the yarn.

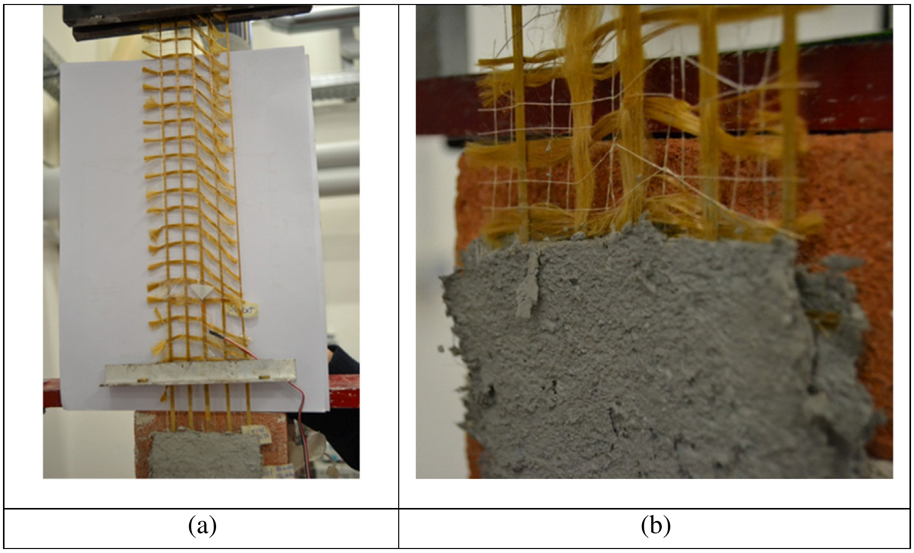
(a)
(b)

Fig. 2. Typical observed failure modes: (a) slippage and (b) tensile failure of the yarns.

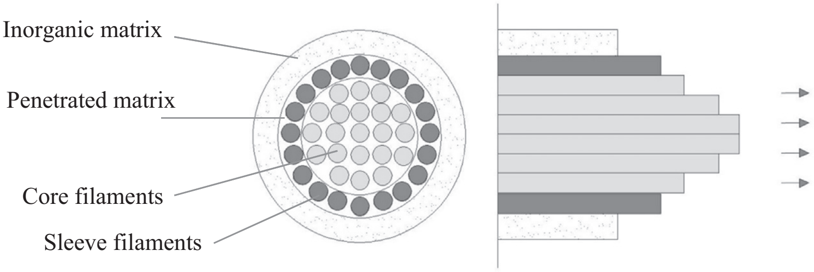

Fig. 3. Telescopic behaviour idealization of a yarn embedded in the matrix.

3. Analytical model for the matrix–fabric debonding

Based on the experimental outcomes, the main aim of the paper is the investigation of the matrix–fabric debonding. Analytical expressions for the load–displacement response and interfacial shear stress distribution at different loading stages are derived considering the effect of the friction phenomena. The main assumptions of the proposed model are:

- The substrate and the matrix are assumed to be not deformable, i.e., just the displacement, u, of the textile is considered. The slip between the yarns and the matrix is then equal to the displacement of the grid.
- The displacement is assumed to be the same in each yarn of the grid and then the external applied load is considered to be equally distributed between the yarns of the textile. This means that the model prediction in terms of the applied load should be multiplied by the number of yarns in the fabric, n_{yarns}, in order to get the actual model response.
- In order to take into account the effect of the telescopic failure mode illustrated in Fig. 3, an effective area should be considered in the model. The effective area is a fraction of the dry yarn area and it should be estimated from the experimental results.
- The yarn is assumed to be linear elastic and no shear among the filaments of the yarn is considered.
- A trilinear shear stress–displacement relationship between the shear stress, τ, at the matrix–textile interface and the yarn displacement, u, is assumed. Details are presented in Section 3.1.

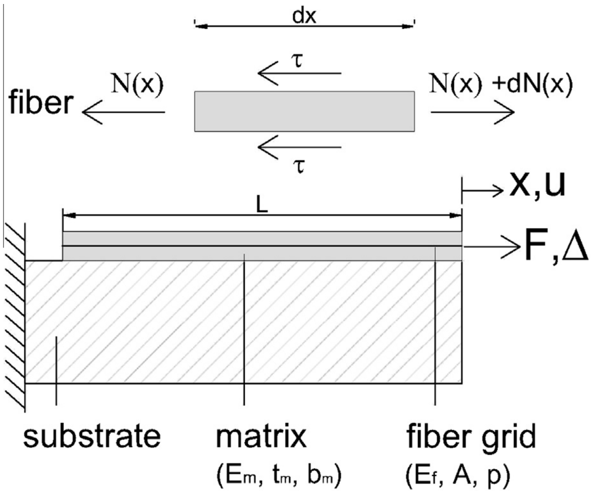

Fig. 4. Pull–push loading scheme and equilibrium of a single yarn.

3.1. Governing equations and bond–displacement law

In Fig. 4 a pull–push loading configuration similar to the one considered in the experimental test is shown. According to the hypotheses stated above, the behaviour of a single yarn of the fabric is investigated. The effective area of the yarn is denoted as A, while p denotes the wet perimeter of the yarn.

The equilibrium of a small length dx of the yarn (see Fig. 4) provides:

$$\tau = \frac{1}{p}\frac{dN}{dx} \tag{1}$$

where N is the axial force of the yarn and τ is the shear stress at the matrix–textile interface which is function, according to the main assumptions of the model, of the yarn displacement, u. Then, compatibility and constitutive relationships for the yarn give:

$$\frac{dN}{dx} = EA\frac{d^2u}{dx^2} \tag{2}$$

where E is the yarn Young's modulus. Inserting Eq. (1) into Eq. (2) one has:

$$\frac{d^2u}{dx^2} - \frac{p}{EA}\tau = 0 \tag{3}$$

The solution of Eq. (3) requires the definition of a reliable interface shear–displacement model. Literature review shows that bilinear models with a linear ascending branch followed by a linear descending branch provide a good approximation of the experimental data. Besides, a friction stage is added in this paper in order to model the friction between the textile and the matrix. In the proposed model, the shear stress behaviour at the textile–mortar interface is then regarded to be tri-linear, as shown in Fig. 5.

In the stage (I) the yarn is completely bonded to the matrix and the shear stress at the interface between yarn and matrix increases proportionally to the yarn displacement, that is $\tau = k_1 u$ and the slip is comprised between 0 and u_{max}. When the maximum shear stress, τ_{max}, is achieved, the softening stage (stage (II)) outsets and the shear stress decreases proportionally to the yarn displacement. In this softening branch the slip is comprised between u_{max} and u_0 and the shear stress at the interface becomes:

$$\tau = -k_2 u + \tau_{max}\left(\frac{k_1 + k_2}{k_1}\right) \tag{4}$$

where k_1 and k_2 are the slopes of the ascending and descending branch, respectively. Finally, the displacement reached at the end of the softening phase is:

$$u_0 = -\frac{\tau_0}{k_2} + \tau_{max}\left(\frac{k_1 + k_2}{k_1 k_2}\right) \tag{5}$$

At the end (stage (III)), the shear stress becomes constant and is equal to the friction τ_0 when the yarn displacement is greater than u_0.

3.2. Evolution of the debonding process

With the shear displacement model described above, Eq. (3) can be solved to evaluate the yarn displacement, u, and the shear stress at the textile–matrix interface, τ. Besides, the axial force, N, in the yarn is evaluated as:

$$N = EA\frac{du}{dx} \tag{6}$$

while the textile displacement, Δ, at the loaded end is equal to $u(0)$ and the applied force, F, is given by $N(0)$ (see Fig. 4). This provides the load–displacement response of the reinforcement. The solution is presented below for the different stages of the textile–matrix interface (elastic, softening and friction) illustrated in Fig. 5. The interfacial shear stress distribution along the yarn is reported in Fig. 6. Note that Fig. 6 refers to the case of a long bond length. The concept of long bond length will be better discussed in the following.

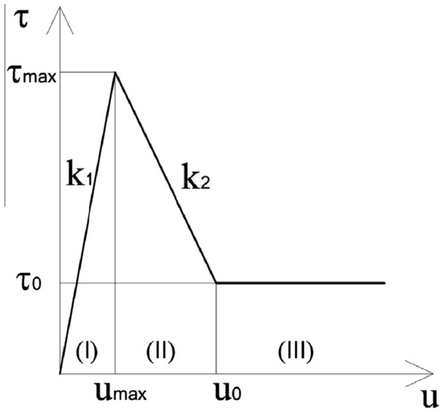

Fig. 5. Shear stress–displacement law at matrix–textile interface.

In Fig. 6, it is shown that, in general, more than one stage may occur at the interface for a given point of the load–displacement relationship. For long bond lengths, the typical normalized load–displacement relationship, $\overline{F} - \overline{\Delta}$, is reported in Fig. 7.

The load–displacement response is characterized by five phases. In the first phase, the response is linear-elastic and the load–displacement curve is represented by the segment O–A. The shear stress distribution along the interface is reported in Fig. 6a and b. At the end of the elastic phase, a portion of the inter-face enters in the softening stage (stage (II) in Fig. 5) while the remaining part is still in the elastic phase (stage (I) in Fig. 5) and the shear stress distribution along the interface is depicted in Fig. 6c and d. The relevant load–displacement curve is represented in Fig. 7 by the segment A–B. At the end of this phase a portion of the interface enters in the friction stage (stage (III) in Fig. 5) while the remaining part is still in the elastic-softening phase and the shear stress distribution along the interface is depicted in Fig. 6e and f. The relevant load–displacement curve is represented in Fig. 7 by the segment B–C. Note that during this phase, the applied force is not constant but still increases due to the friction phenomenon. This is an innovative aspect of the model compared to the ones available in the literature. At the end of the elastic-softening-friction phase, there is no elastic stage at the interface and the shear stress distribution is represented by Figs. 6g and h. The relevant load–displacement curve is represented in Fig. 7 by the segment C–D and it is associated to a snap-back phenomenon. At the end of this softening-friction phase the shear stress is equal to the frictional stress along the whole interface. The relevant load–displacement curve is represented in Fig. 7 by the segment D–E.

As stated above, Fig. 7 represents the load–displacement curve for long bond lengths. For a short bond length, the situation is different since the shear distribution at the end of the elastic-softening phase is represented by Fig. 8a. There is no elastic stage and the interface is in the softening stage (stage (II) in Fig. 5) along the whole length. At the end of the softening phase the shear distribution is reported in Fig. 8b. Then the shear stress distribution evolves as for long bond lengths with the softening-friction phase (see Fig. 6h).

The typical normalized load–displacement relationship, $\overline{F} - \overline{\Delta}$, for a short bond length is reported in Fig. 9.

In the load–displacement curve, comparing Figs. 7 and 9 it should be observed that for short bond lengths the friction phenomenon (segment B–C in Fig. 7) is not present and the load decreases just after point B (segment B–C in Fig. 9). Besides, no snap-back phenomenon is observed.

The solution of Eq. (3) is presented in the following with reference to the different phases listed above.

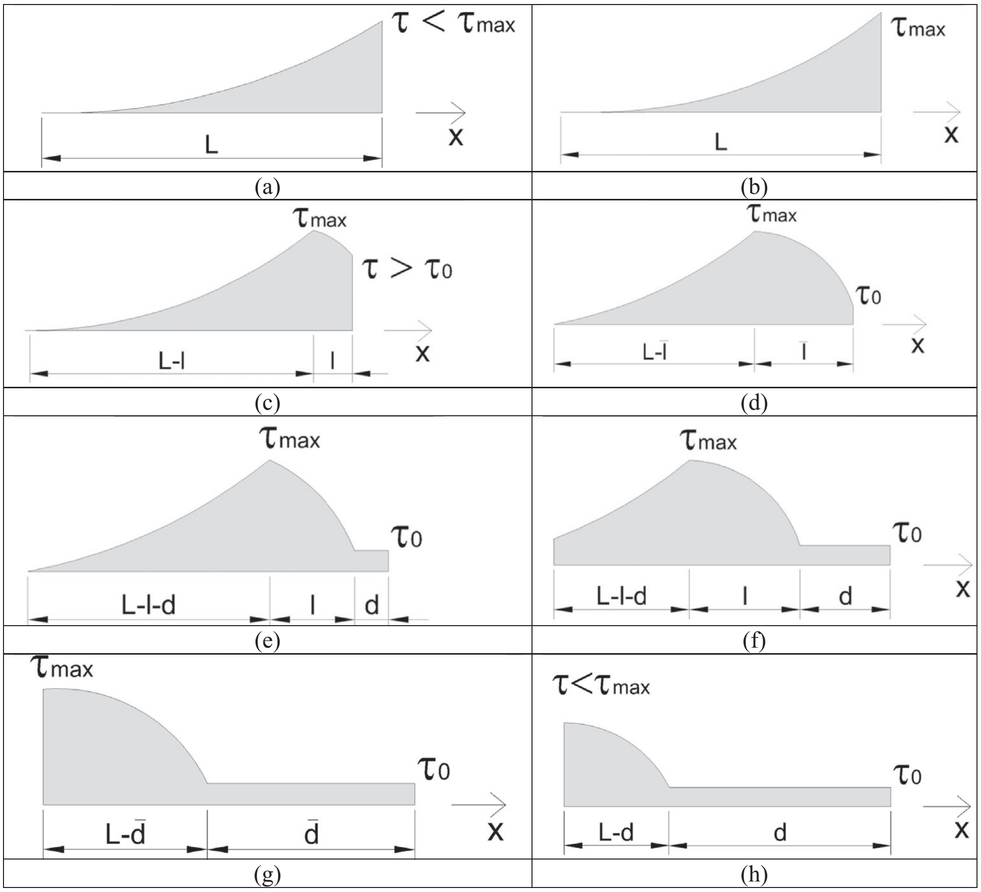

(a) (b)

(c) (d)

(e) (f)

(g) (h)

Fig. 6. Shear stress distribution at matrix–textile interface for long bond lengths: (a) and (b) elastic phase, (c) and (d) elastic-softening phase, (e) and (f) elastic-softening-debonding phase, (g) and (h) softening-debonding phase.

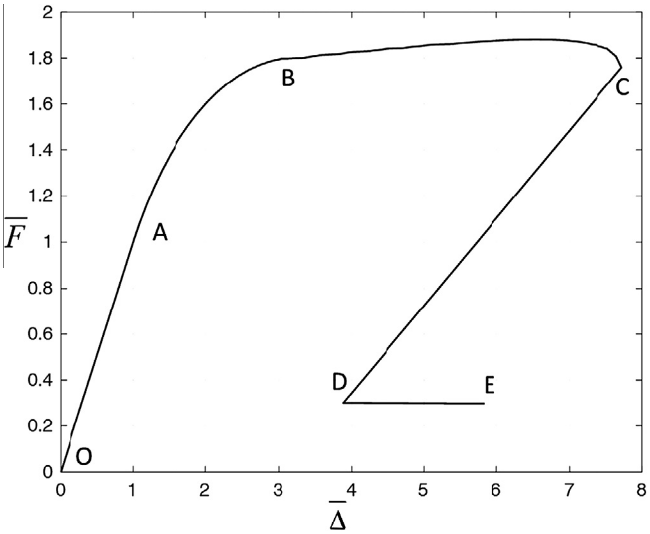

Fig. 7. Typical normalized load–displacement curve for a long bond length.

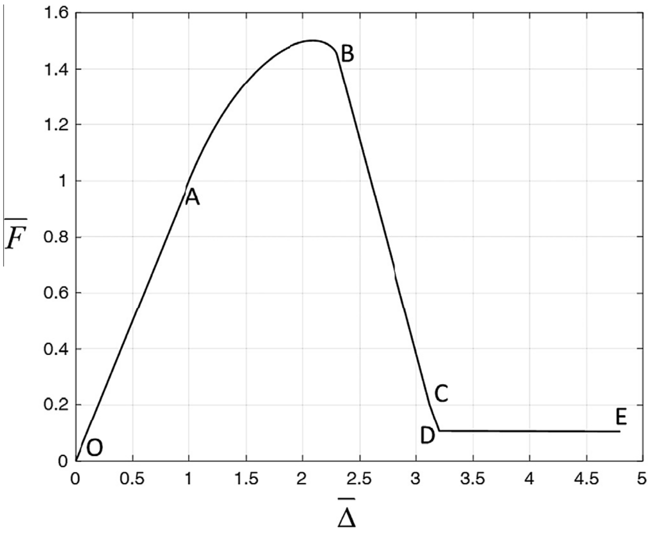

Fig. 9. Typical normalized load–displacement curve for a short bond length.

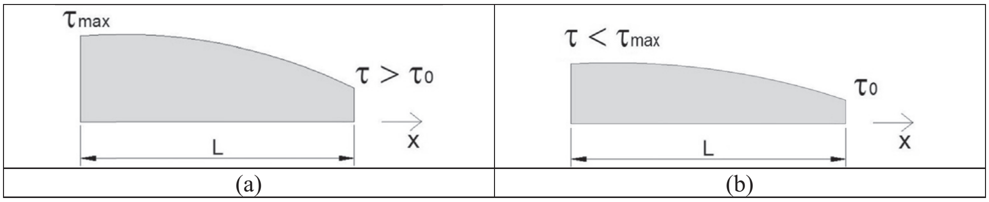

(a) (b)

Fig. 8. Shear stress distribution at matrix–textile interface for a short bond length: (a) and (b) softening phase.

3.2.1. Elastic phase

In the first phase, $\tau = k_1 u$ and Eq. (3) becomes:

$$\frac{d^2u}{dx^2} - \lambda^2 u = 0 \tag{7}$$

where:

$$\lambda = \sqrt{\frac{pk_1}{EA}} \tag{8}$$

The boundary conditions are:

$$\begin{aligned} N &= 0 \quad \text{at} \quad x = -L \\ N &= F \quad \text{at} \quad x = 0 \end{aligned} \tag{9}$$

With these boundary conditions the solution of Eq. (7) is:

$$u = \frac{F}{\lambda EA} \frac{\cosh(\lambda(L + x))}{\sinh(\lambda L)} \tag{10}$$

The shear stress distribution along the interface is given in Fig. 6a. For the yarn displacement, Δ, at the loaded end one has from Eq. (10):

$$\Delta = \frac{F}{\lambda EA \tanh(\lambda L)} \tag{11}$$

Eq. (11) provides the expression for the load–displacement curve in the elastic phase. At the end of the elastic phase, when the shear stress reaches the maximum tangential stress τ_{max} at $x = 0$ (see Fig. 6b), the displacement, u, in the yarn is computed from Eq. (10) as:

$$u = \frac{\tau_{max}}{k_1} \frac{\cosh[\lambda(L + x)]}{\cosh(\lambda L)} \tag{12}$$

while making use of Eq. (6), the axial force, N, in the yarn is equal to:

$$N = \frac{p \cdot \tau_{max}}{\lambda} \cdot \frac{\sinh[\lambda(L + x)]}{\cosh(\lambda L)} \tag{13}$$

At the loaded end one has from Eq. (13):

$$F = \frac{p \cdot \tau_{max}}{\lambda} \tanh(\lambda L) \tag{14}$$

The displacement at the end of the elastic phase is equal to u_{max} and since $\tau_{max} = k_1 \cdot u_{max}$, the elastic stiffness of the grid, K_e, is evaluated from Eq. (14) as:

$$K_e = \frac{p \cdot k_1}{\lambda} \tanh(\lambda L) \cdot n_{yarns} \tag{15}$$

where n_{yarns} is the number of yarns in the fabric.

3.2.2. Elastic-softening phase

Once the shear stress reaches τ_{max}, softening starts at the loaded end and a portion of the textile–matrix interface enters in the softening state, while the other remains in the elastic state (see Fig. 6c). The length of the softening part is denoted by l and the load continues to increase as l increases. At the end of the elastic part ($x = -l$), the load is given by Eq. (14) for a bond length equal to ($L-l$):

$$F = \frac{p \cdot \tau_{max}}{\lambda} \cdot \tanh[\lambda(L - l)] \tag{16}$$

In the softening phase, for $-l < x < 0$, the shear stress–displacement relation is governed by Eq. (3) while the shear stress, τ, is given by Eq. (4). One has for the governing equation:

$$\frac{d^2u}{dx^2} + \omega^2 u = \frac{p \cdot \tau_{max}}{EA} \left(\frac{k_1 + k_2}{k_1} \right) \tag{17}$$

where:

$$\omega = \sqrt{\frac{pk_2}{EA}} \tag{18}$$

The boundary conditions are:

$$\begin{aligned} u &= \frac{\tau_{max}}{k_1} \quad \text{at} \quad x = -l \\ N &= \frac{p \cdot \tau_{max}}{\lambda} \cdot \tanh[\lambda(L - l)] \quad \text{at} \quad x = -l \end{aligned} \tag{19}$$

Eq. (19) represents the continuity conditions at $x = -l$ where the axial force in the yarn is given by Eq. (16). With these boundary conditions the solution of Eq. (17) is:

$$u = \frac{\tau_{max}}{k_2} \frac{\sin(\omega x + \varphi)}{\sin(\omega l - \varphi)} + \frac{k_1 + k_2}{k_1 k_2} \tau_{max} \tag{20}$$

where:

$$\varphi = \omega l - \text{arctg} \frac{\lambda}{\omega \cdot \tanh[\lambda(L - l)]} \tag{21}$$

while making use of Eq. (6), the axial force, N, in the softening part of the yarn is equal to:

$$N = \frac{p \cdot \tau_{max}}{\omega} \frac{\cos(\omega x + \varphi)}{\sin(\omega l - \varphi)} \tag{22}$$

The yarn displacement of the loaded end, $u(0)$, is equal to Δ, and then one has from Eqs. (20) and (21):

$$\Delta = \frac{\tau_{max}}{k_2} \frac{\sin\varphi}{\sin(\omega l - \varphi)} + \frac{k_1 + k_2}{k_1 k_2} \cdot \tau_{max} \tag{23}$$

The axial force at the loaded end, $N(0)$, is equal to F, and one has from Eqs. (21) and (22):

$$F = \frac{p \cdot \tau_{max}}{\omega} \frac{\cos(\varphi)}{\sin(\omega l - \varphi)} \tag{24}$$

Eqs. (21), (23) and (24) provide the parametric expression for the load–displacement curve in the elastic-softening phase. The numerical solution of Eqs. (21) and (24) provides the length of the softening phase, l, to be inserted in Eq. (23) in order to evaluate the yarn displacement at the loaded end. When $\tau(0) = \tau_0$, the elastic-softening phase is concluded and the shear stress distribution along the interface is showed in Fig. 6d.

3.2.3. Elastic-softening-friction phase

When the shear stress τ_0 is reached at the loaded end, the shear stress at the textile–matrix interface cannot decrease due to the friction phenomena in the debonded part. In this phase the reinforcement bond length could be considered divided in three parts, that are the elastic, softening and friction ones. The length of the debonded part is denoted by d while l indicates the length of the softening part. The length of the elastic part is then equal to L–l–d (see Fig. 6e). In the friction phase the axial force for unit length is equal to $p \cdot \tau_0$ and then the axial force in the yarn at $x = -d$ is equal to $F - p \cdot \tau_0 \cdot d$. Eqs. (21) and (24) are still valid in the elastic-softening portion and then one has by replacing L with (L–d):

$$F - p \cdot \tau_0 \cdot d = \frac{p \cdot \tau_{max}}{\omega} \frac{\cos(\varphi)}{\sin(\omega l - \varphi)} \tag{25}$$

where now:

$$\varphi = \omega l - \text{arctg} \frac{\lambda}{\omega \cdot \tanh[\lambda(L - d - l)]} \tag{26}$$

Additionally, the yarn displacement in $x = -d$ is equal to u_0 and then one has from Eqs. (23) and (26):

$$-\frac{\tau_0}{k_2} = \frac{\tau_{max}}{k_2}\frac{\sin\varphi}{\sin(\omega l - \varphi)} \tag{27}$$

Eqs. (25) and (27) should be solved numerically to evaluate the length of the debonding part, *d*, and the softening part, *l*. The displacement at the loaded end is finally evaluated as:

$$\Delta = u_0 + \frac{F \cdot d}{EA} - \frac{p \cdot \tau_0}{2EA}d^2 \tag{28}$$

As debonding propagates, the peak shear stress, τ_{max}, moves towards the reinforcement end and the situation is reported in Fig. 6f. As long as the elastic phase is completely developed (see Fig. 6e), the load increases while, on the reverse, if the elastic part is truncated (see Fig. 6f) the load decreases. When $\tau(-L) = \tau_{max}$, the elastic-softening phase is concluded and the shear stress distribution along the interface is showed in Fig. 6g.

3.2.4. Softening-friction phase

When the shear stress reaches the maximum value τ_{max} at the reinforcement end, the softening-friction phase begins (see Fig. 6g). The bond–displacement relationship is governed by Eq. (17) and the boundary conditions are:

$$\begin{aligned} &N = 0 \quad \text{at} \quad x = -L \\ &N = F - p \cdot \tau_0 \cdot d \quad \text{at} \quad x = -d \end{aligned} \tag{29}$$

Eq. (17) can be rewritten as:

$$\frac{d^2u}{dx^2} + \omega^2 u = \tau_{max}\omega^2\frac{k_1 + k_2}{k_1k_2} \tag{30}$$

The solution of Eq. (30) with the above boundary conditions is:

$$\begin{aligned} u = {} & \frac{F - p \cdot \tau_0 \cdot d}{\omega EA}\sin[\omega(x + d)] - \frac{F - p \cdot \tau_0 \cdot d}{\omega EA}\frac{\cos[\omega(x + d)]}{\tan[\omega(L - d)]} \\ & + \tau_{max}\frac{k_1 + k_2}{k_1k_2} \end{aligned} \tag{31}$$

In $x = -d$ the yarn displacement should be equal to u_0 and then from Eq. (31) one has:

$$F - p \cdot \tau_0 \cdot d = \frac{p \cdot \tau_0}{\omega} \cdot \tan[\omega(L - d)] \tag{32}$$

The displacement at the loaded end is again provided by Eq. (28). At the end of this phase $d = L$ and then the displacement, Δ, of the loaded end is equal to:

$$\Delta = u_0 + \frac{p \cdot \tau_0}{2EA}L^2 \tag{33}$$

3.2.5. Friction phase

At the end of the softening-friction phase, the displacement Δ of the loaded end is given by Eq. (33) while $F = p \cdot \tau_0 \cdot L$. As the displacement increase the load is given by:

$$F = p \cdot \tau_0 \cdot (L - \Delta) \tag{34}$$

3.2.6. Softening phase for short bond lengths

For short bond lengths, the shear stress distribution at the end of the elastic softening phase is reported in Fig. 8a and the interface is in the softening regime along the whole length. The governing equation is provided by Eq. (30), while the corresponding boundary conditions are:

$$\begin{aligned} &N = 0 \quad \text{at} \quad x = -L \\ &N = F \quad \text{at} \quad x = 0 \end{aligned} \tag{35}$$

The solution is:

$$u = \frac{F}{\omega EA}\sin(\omega x) - \frac{F}{\omega EA}\frac{\cos(\omega x)}{\tan(\omega L)} + \tau_{max}\frac{k_1 + k_2}{k_1k_2} \tag{36}$$

The displacement of the loaded end, Δ, is evaluated by setting $x = 0$ in Eq. (36):

$$\Delta = -\frac{F}{\omega EA\tan(\omega L)} + \tau_{max}\frac{k_1 + k_2}{k_1k_2} \tag{37}$$

The shear stress distribution at the end of this phase is reported in Fig. 8b. Finally, the shear stress distribution evolves as in Fig. 6h for the case of long bond lengths.

4. Discussion and validation of the analytical model

In this Section, the main results of the analytical model introduced in Section 3 are first discussed. Then the outcomes of the experimental tests illustrated in Section 2 are used to validate the proposed analytical model.

4.1. Discussion of the proposed analytical model

In the following, the main results of the analytical model are discussed in terms of elastic and elastic-softening effective bond length, optimal bond length and limiting load level at the most significant points of the load–displacement curve in Figs. 7 and 9.

From Fig. 6b it is firstly observed that in the elastic phase only a portion of the interface is significantly stressed, while the stress elsewhere is quite small. In the literature [22] an elastic effective bond length, $L_{eff,e}$, is then defined as the bond length required to mobilize a shear stress which offers a total resistance equal to 97% of the applied load for a joint with an infinite bond length. Since $\tanh(2) \simeq 0.97$ one has:

$$L_{eff,e} = \frac{2}{\lambda} \tag{38}$$

and if $L > L_{eff,e}$ Eq. (14) becomes:

$$F = \frac{p \cdot \tau_{max}}{\lambda} \tag{39}$$

This load level corresponds to point A in Figs. 7 and 9.

On the other hand, it should be noted that Fig. 6d holds if $\bar{l} \leqslant L$, that is if the bond length is long enough to completely develop the softening phase. The corresponding elastic-softening effective bond length, $L_{eff,es}$, is evaluated by setting $l = L$ and $\Delta = u_0$ in Eq. (23). In this case, from Eq. (21), one has $\varphi = \omega L - \pi/2$ and then:

$$\sin\left(\omega L_{eff,es} - \frac{\pi}{2}\right) = -\frac{\tau_0}{\tau_{max}} \tag{40}$$

The solution of Eq. (40) gives for $L_{eff,es}$:

$$L_{eff,es} = \frac{\arcsin\left(-\frac{\tau_0}{\tau_{max}}\right) + \frac{\pi}{2}}{\omega} \tag{41}$$

From Fig. 6d an optimal bond length, L_{opt}, could be also defined as the bond length which is required to completely develop the elastic-softening phase. It is evaluated by using Eqs. (38) and (41) as:

$$L_{opt} = \frac{2}{\lambda} + \frac{\arcsin\left(-\frac{\tau_0}{\tau_{max}}\right) + \frac{\pi}{2}}{\omega} \tag{42}$$

For $L \geqslant L_{opt}$ (long bond length), the load level at the end of elastic-softening phase converges to:

$$F = \frac{p \cdot \tau_{max}}{\omega}\sqrt{1 + \frac{\omega^2}{\lambda^2}} \tag{43}$$

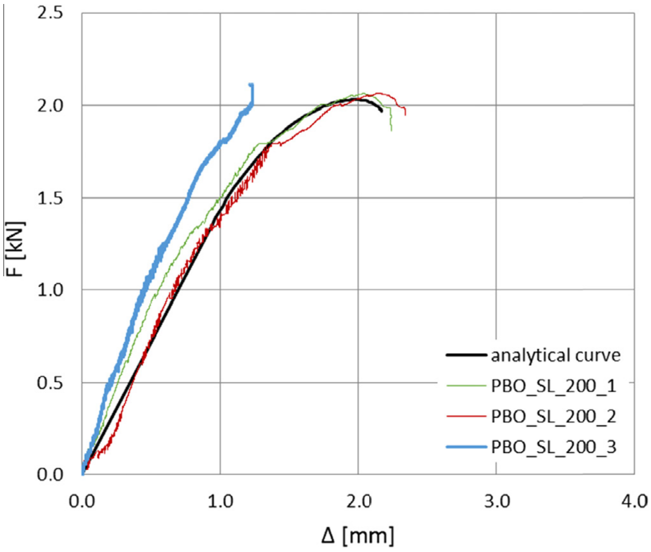

Fig. 10. Comparison between experimental and analytical load–displacement curves.

This load level corresponds to point B in Fig. 7. It should be noted that for $L \geqslant L_{opt}$ the load increases from point B to C during the elastic-softening-friction phase due to the friction phenomenon. It is not possible to evaluate the load level corresponding to point C in a closed form, but for design purposes and a realistic value of the friction parameter τ_0, Eq. (43) provides a reasonable conservative estimation of the joint strength.

Finally, if $L < L_{eff,es}$ (short bond length) the load level at the end of the elastic-softening phase converges to:

$$F = \frac{p \cdot \tau_{max}}{\omega} \sin(\omega L) \tag{44}$$

This load level corresponds to point B in Fig. 9. This load level is very close to the peak load and it can be used in practical applications as a reasonable estimation of the joint strength. For $L < L_{eff,es}$ the load decreases from point B to point C during the softening-friction phase. The load level corresponding to point C is provided by setting $u = u_0$ in Eq. (36). One has then:

$$F = \frac{p \cdot \tau_0}{\omega} \tan(\omega L) \tag{45}$$

4.2. Experimental validation of the proposed analytical model

The experimental curves used in this work were obtained as described in Section 2. The bond length was equal to 200 mm, the Young's modulus of the yarn was of 217 GPa while the dry area of the yarn was of 0.221 mm^2. The relevant load–displacement plot is reported in Fig. 10.

When the maximum load is reached, the load–slip curves tend to be characterized by a decreasing phase. No friction phenomenon was observed and then the joint should be classified as short length joint. The typical load–displacement curves are then similar to the one in Fig. 9. The decreasing phase was not recognizable during the experimental tests due to the testing machine characteristics.

The bond parameters k_1, k_2 and τ_{max} are experimentally calibrated using data of key points of the experimental load–displacement response. At first, the displacement, $\overline{u}_A$, and the load for a single yarn, $\overline{F}_A$, at the elastic limit (point A in Fig. 9) are determined from the experimental load–displacement plot. For $L > L_{eff,e}$, the load at the elastic limit is given by Eq. (39). Making use of Eq. (8), with $\tau_{max} = k_1 \cdot \overline{u}_A$ one has then:

$$\overline{F}_A = \frac{p \cdot k_1 \cdot \overline{u}_A}{\sqrt{\frac{p \cdot k_1}{EA}}} \tag{46}$$

Solving Eq. (46), the slope k_1 of the elastic part of the bond–dis-placement relationship is:

$$k_1 = \frac{\overline{F}^2}{\overline{u}^2 \cdot p \cdot EA} \tag{47}$$

and finally $\tau_{max} = k_1 \cdot \overline{u}$. In order to calibrate the slope, k_2, of the softening branch of the bond–displacement relationship, point B in Fig. 9 should be detected on the experimental load–displacement plot. For a short bond length, the corresponding load level at the end of the elastic-softening branch is given by Eq. (44). Denoting with F_B the load level for a single yarn corresponding to point B, one has inserting Eq. (18) in Eq. (44):

$$\overline{F}_B = \frac{p \cdot \tau_{max}}{\sqrt{\frac{pk_2}{EA}}} \sin \sqrt{\frac{pk_2}{EA}} L \Bigg) \tag{48}$$

Eq. (48) should be solved numerically to evaluate the slope k_2 of the softening branch for short bond lengths. The above calibrated parameters k_1, τ_{max} and k_2 allow the evaluation of the load–displacement curve up to the end of the elastic-softening phase. The values of the bond parameters for FRCM materials used in the experimental campaign are reported in Table 1.

Note that with the model parameters listed in Table 2, the elastic-softening effective bond length, $L_{eff,es}$, can be evaluated by using Eq. (41) as 266 mm. Such value is greater than the bond length (200 mm) and then the joint can be effectively considered as a short joint. According to what reported in Section 3, from the experimental results, the effective area of the yarn was estimated equal to 0.167 mm^2, that is 75% of the dry yarn area, leading to a good correspondence between the model and the experimental results, as shown in Fig. 10.

With reference to the friction shear stress τ_0, it should be noted that the estimation of this parameter is straightforward if the corresponding displacement, u_0, is estimated from the experimental load–displacement curve. This corresponds to point C in Fig. 9 and denoting this value with $\overline{u}_{0,C}$, one has from Eq. (5):

$$\tau_0 = -k_2 \cdot \overline{u}_{0,C} + \tau_{max} \frac{k_1 + k_2}{k_1} \tag{49}$$

From the experimental point of view, the estimation of $\overline{u}_{0,C}$ is difficult since it is troublesome to plot the descending branch of the load–displacement curve. In the experimental tests described in Section 2 this was not possible and therefore the comparison between experimental and analytical results in Table 2 is limited to elastic stiffness, load at the elastic limit and peak loads.

In Table 2 the elastic stiffness is evaluated using Eq. (15) while the load at the elastic limit was computed with Eq. (14). The peak load is estimated as the load level corresponding to point B in Fig. 9 as given by Eq. (44). In Table 2, the agreement between the experimental values and the analytical findings is good.

5. Parametric analysis

In this section the effect of bond length, cohesive bond–slip law parameters and friction on the load–displacement response are analysed using the experimental identified model parameters, k_1,

Table 1
Bond parameters evaluation.

Material	τ_{max} [MPa]	k_1 [MPa/mm]	k_2 [MPa/mm]
PBO-FRCM	1.7	1.8	0.8

Table 2
Comparison between experimental and analytical results.

Specimen	Experimental results			Analytical results		
	Elastic stiffness [kN/mm]	Elastic limit load [kN]	Peak load [kN]	Stiffness [kN/mm]	Elastic limit load [kN]	Peak load [kN]
PBO-FRCM	1.33–1.78	0.95–1.61	1.69–2.12	1.43	1.35	1.96

Table 3
Layout of the parametric analysis.

Case	Model parameters					Remarks
	L [mm]	k_1 [MPa/mm]	τ_{max} [MPa]	k_2 [MPa/mm]	τ_0 [MPa]	
1	200	1.8	1.7	0.8	0.1	Effect of bond length
2	400	1.8	1.7	0.8	0.1	
3	600	1.8	1.7	0.8	0.1	
4	200	1.8	1.7	0.8	0.1	Effect of shear stress–displacement law parameters
5	200	1.8	1.7	1.6	0.1	
6	200	1.8	1.7	2.4	0.1	
7	600	1.8	1.7	0.8	0.1	Effect of the friction parameters
8	600	1.8	1.7	0.8	0.2	
9	600	1.8	1.7	0.8	0.3	

k_2, τ_{max}, τ_0 and the experimental joint length L as reference. The selected model parameters are listed in Table 3 and they are the bond length, L, the slope of the softening branch of the bond–displacement relationship, k_2, and the friction, τ_0. That is, except for the parameter under investigation, the values of all other parameters (the yarn section, wet perimeter and the slope k_1 of the elastic part of the bond–displacement relationship) are the same as in previous section. The reference case in Table 3 is represented by Case 1.

5.1. Effect of bond length

The effect of bond length on the load–displacement response is illustrated in Fig. 11. Three different bond lengths were selected: 200 mm, 300 mm and 600 mm. All the other model parameters are kept constant. The bond–displacement relationship is reported in Fig. 11a while the load–displacement curve is plotted in Fig. 11b.

It is evident that, increasing the bond length, the elastic stiffness and the elastic limit tend to a constant value. Besides, as far as the bond length increases, the load at the end of the elastic-softening branch tends to a constant value. Instead, the maximum load increases with the bond length due to the friction effect. It is worth noting that it is not possible to define an effective bond length, that is a threshold length beyond which the maximum load is achieved. The bond length has finally a great influence on the behaviour of the load–displacement curve. A longer bond length, in fact, improves the joint ductility, that is, the displacement of the joint at the loaded end increases together with the ultimate load. In particular, the increment of the ultimate load is due to friction effect and then clearly increases with the bond length. When the bond length increases, snap-back is also detected, that is, for a short bond length softening is observed in the load–displacement curve while for a longer bond snap-back is detected.

5.2. Effect of the cohesive bond–displacement law parameters

The effect of the cohesive bond–slip law parameters on the load–displacement response is illustrated in Fig. 12.

While the slope k_1 of the elastic branch is kept constant, three different values for the slope k_2 of the softening branch were

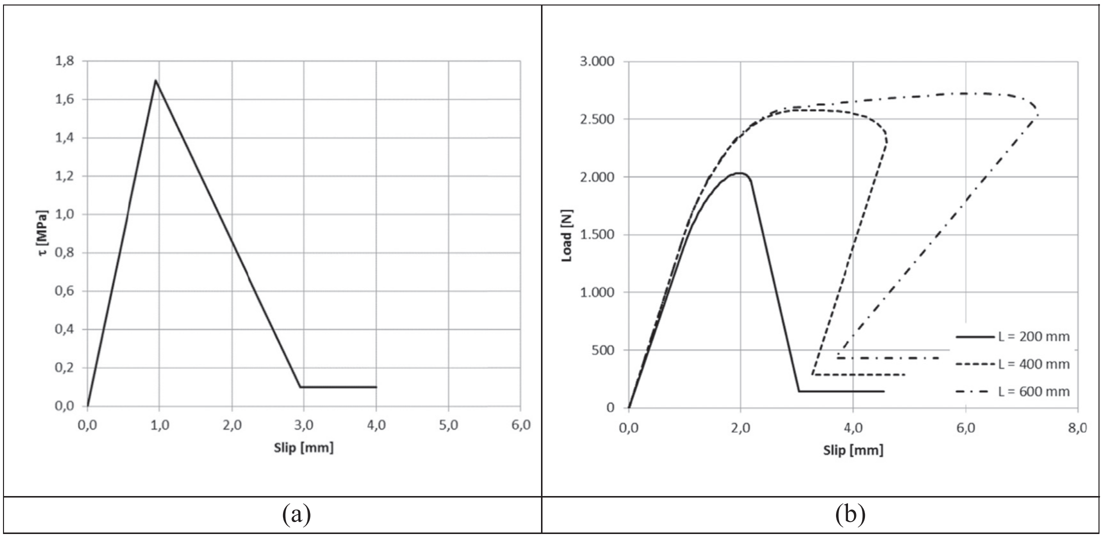

(a) (b)

Fig. 11. Effect of bond length on the load–displacement curve: (a) shear stress–displacement law and (b) load–displacement curves.

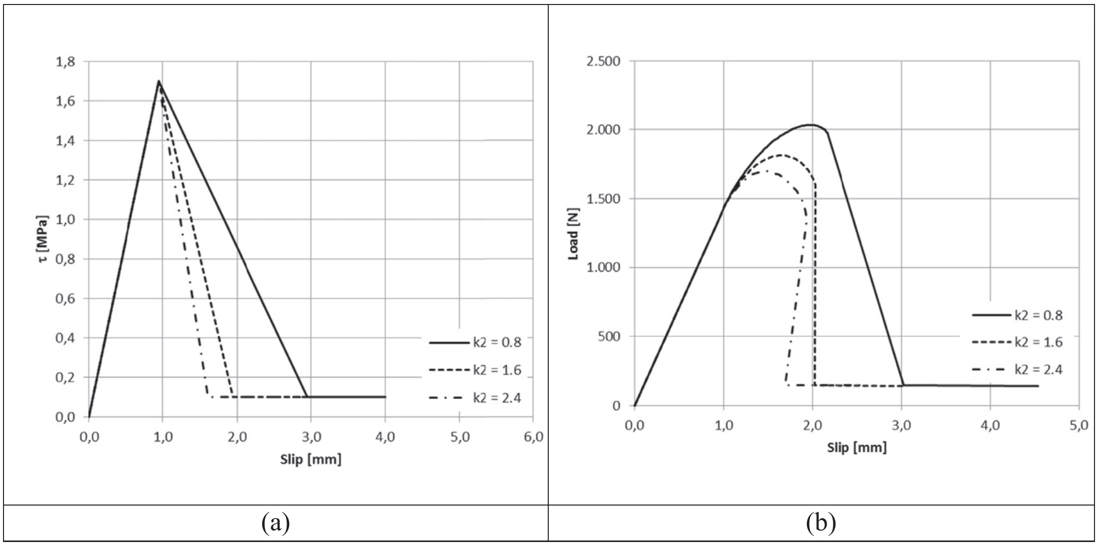

(a) (b)

Fig. 12. Effect of shear stress–displacement law parameters on the load–displacement curve: (a) shear stress–displacement law and (b) load–displacement curves.

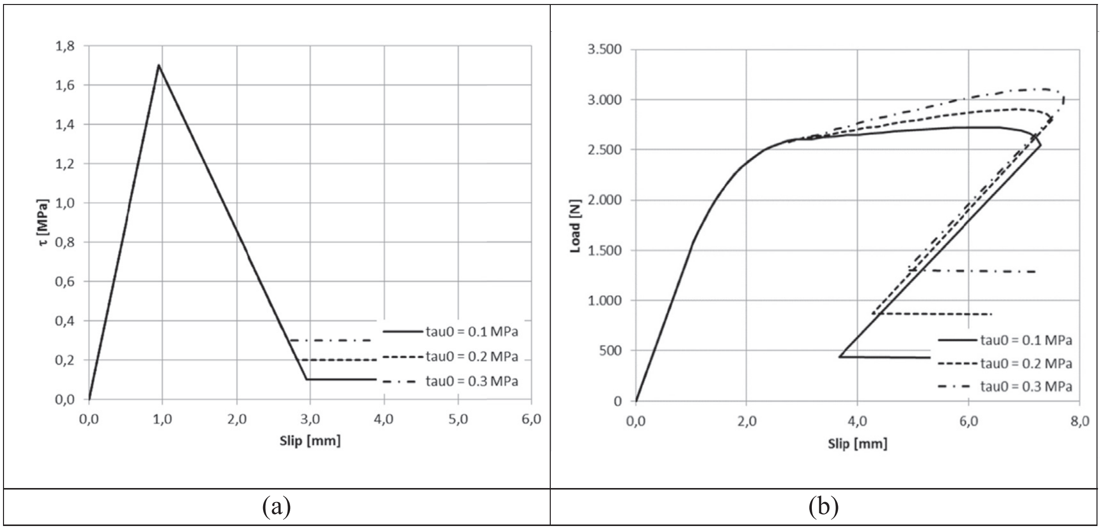

(a) (b)

Fig. 13. Effect of the friction parameters on the load–displacement curve: (a) shear stress–displacement law and (b) load–displacement curves.

selected, that is, 0.8 MPa/mm, 1.6 MPa/mm and 2.4 MPa/mm. All the other model parameters are kept constant. The bond–displacement relationship is reported in Fig. 12a while the load–displacement curve is plotted in Fig. 12b. Since the maximum shear stress τ_{max} and the bond length L are kept constant, the variation of the slope of the softening branch has no influence on the elastic stiffness and on the elastic limit. Although the maximum shear stress τ_{max} is the same for all the curves, it is evident from Fig. 12b that the presence of a softening branch in the bond–slip law provides a strength increment beyond the elastic limit. This holds also for short bond lengths where the effect of friction is not present. The parameter k_2 has an influence also on the beha-viour of the load–displacement curve since the snap-back instabil-ity tends to disappear as the slope of the softening branch increases.

5.3. Effect of the friction parameter

The effect of the friction parameter on the load–displacement response is illustrated in Fig. 13.

Three different values of the friction shear stress τ_0 were selected, that is, 0.1 MPa/mm, 0.2 MPa/mm and 0.3 MPa/mm. All the other model parameters are kept constant. The joint length was selected equal to 600 mm in order to emphasize the effect of the friction parameter on the load–displacement curves. The bond–displacement relationship is reported in Fig. 13a while the load–displacement curve is plotted in Fig. 13b. The friction param-eter has no effect on the elastic stiffness and on the elastic limit while it has an evident effect on the joint ductility, i.e., the maxi-mum displacement increases with the friction parameter. The parameter τ_0 has also a clear influence on the behaviour of the load–displacement curve since snap-back instability is always observed.

6. Conclusions

In this paper a cohesive interface crack model was presented for the matrix–textile debonding in FRCM materials. At first, from the experimental evidence it is recognized that the failure mode of FRCM materials bonded to the substrate is due to yarn tensile failure or to slippage of the textile. A closed form solution of the proposed analytical model was presented to predict the entire debonding process of the textile from the matrix. The solution was computed considering a realistic tri-linear bond–displacement law where a constant shear stress branch was added to the standard linear and softening ones. The constant shear stress was added to model the friction phenomenon observed in experimental tests described in the literature. It takes into account the interlocking between the textile and the matrix which gives an additional load increment at the end of the elastic-softening phases. The solution provides theoretical bases to understand the behaviour of the joint between FRCM materials and the substrate. In particular, different typical load–displacement relationships are identified and discussed for long and short joint lengths. Besides, analytical solutions for the elastic and elastic-softening effective bond length, optimal bond length and limiting load level at the most significant points of the load–displacement curve are provided. Based on the results and discussion presented in the paper, the following conclusions may be drawn:

1. The proposed tri-linear bond–displacement law permits to model the friction phenomena observed in the literature. This has a marginal influence on the peak loads but it has a significant effect on the joint ductility.
2. When the joint length increases, the joint ductility grows.
3. The maximum load increases with the bond length due to the friction effect. It is then worth noting that it is not possible to define an effective bond length, that is, a threshold length beyond which the maximum load is achieved.
4. When the bond length increases, snap-back is also observed, that is, for a short bond length softening is noticed in the load–displacement curve while for a longer bond snap-back is detected.
5. The presence of a softening branch in the bond–slip law provides a strength increment beyond the elastic limit. In particular, the higher the slope of the softening branch, the higher the joint strength. This has also an influence on the behaviour of the load–displacement curve since snap-back instability tends to disappear as the slope of the softening branch increases.
6. The analytical solution provides also a method for the identification of the bond–displacement law parameters using the data of key points of the load–displacement relationship. The predictions are based on the identified bond–displacement law and provide a load–displacement relationship in close agreement with experimental results.

Acknowledgements

The experimental tests were performed at the Material Testing Laboratory of the Politecnico di Milano. The financial support of the Politecnico di Milano is gratefully acknowledged. Thanks are also expressed to Ruredil S.p.A. for providing the reinforcing materials.

References

[1] Nanni A. FRCM strengthening – a new tool in the concrete and masonry repair toolbox. Concr Int: Des Constr 2012;34(4):43–9.
[2] Orlowsky J, Raupach M. Durability model for AR-glass fibres in textile reinforced concrete. Mater Struct 2008;41(7):1225–33.
[3] Butler M, Mechtecherine V, Hemplel S. Durability of textile reinforced concrete made with AR glass fibre: effect of matrix composition. Mater Struct 2010;43:1351–68.
[4] Pellegrino C, D'Antino T. Experimental behaviour of existing precast prestressed reinforced concrete elements strengthened with cementitious composites. Compos B 2013;55:31–40.
[5] D'Ambrisi A, Focacci F, Caporale A. Strengthening of masonry-unreinforced concrete railway bridges with PBO-FRCM materials. Compos Struct 2013;102:193–204.
[6] Corradi M, Borri A, Castori G, Sisti R. Shear strengthening of wall panels through jacketing with cement mortar reinforced by GFRP grids. Compos B 2014;64:33–42.
[7] Barhum R, Mechtecherine V. Influence of short dispersed and short integral glass fibres on the mechanical behaviour of textile-reinforced concrete. Mater Struct 2013;46:557–72.
[8] Contamine R, Junes A, Si Larbi A. Tensile and inplane shear behavior of textile reinforced concrete: analysis of a new multiscale reinforcement. Constr Build Mater 2014;51:405–41.
[9] Valluzzi MR, Oliveira DV, Caratelli A, Castori G, Corradi M, de Felice G, et al. Round robin test for composite-to-brick shear bond characterization. Mater Struct 2012;45(12):1761–91.
[10] de Felice G, De Santis S, Garmendia L, Ghiassi B, Larrinaga P, Lourenco PB, et al. Mortar-based systems for externally bonded strengthening of masonry. Mater Struct 2013;47(12):2021–37.
[11] D'Ambrisi A, Feo L, Focacci F. Experimental analysis on bond between PBO-FRCM strengthening materials and concrete. Compos B 2012;44(1):524–32.
[12] Malena M, de Felice G. Debonding of composites on a curved masonry substrate: experimental results and analytical formulation. Compos Struct 2014;112:194–206.
[13] Valluzzi MR, Tinazzi D, Modena C. Shear behavior of masonry panels strengthened by FRP laminates. Constr Build Mater 2002;16:409–16.
[14] Lu XZ, Teng JG, Ye LP, Jiang JG. Bond–slip models for FRP sheets/plates bonded to concrete. Eng Struct 2005;27(4):920–37.
[15] Camli US, Binici B. Strength of carbon fiber reinforced polymers bonded to concrete and masonry. Constr Build Mater 2007;21:1431–46.
[16] CNR-DT 200 R1/2013. Guide for the design and construction of externally bonded FRP systems for strengthening existing structures. Materials, RC and PC structures, masonry structures. Italian National Research Council; 2013.
[17] Yuan H, Wu Z. Interfacial fracture theory in structures strengthened with composite of continuous fiber. In: Proc., symp. of China and Japan: science and technology of 21st century, Tokyo; 1999.
[18] Panizza M, Garbin E, Valluzzi MR, Modena C. Bond behaviour of CFRP and GFRP laminates on brick masonry. In: D'Ayala D, Fodde E, editors. Structural analysis of historic construction: preserving safety and significance. London, UK: Taylor & Francis Group; 2008.
[19] Ceroni F, Ferracuti B, Pecce M, Savoia M. Assessment of a bond strength model for FRP reinforcement externally bonded over masonry blocks. Compos B 2014;61:147–61.
[20] Colombi P, Fava G, Poggi C. End debonding of CFRP wraps and strips for the strengthening of concrete structures. Compos Struct 2014;111(1):510–21.
[21] D'Antino T, Sneed LH, Carloni C, Pellegrino C. Matrix–fiber bond behavior in PBO FRCM composites: a fracture mechanics approach. Eng Fract Mech 2014;117:94–111.
[22] Carozzi FG, Colombi P, Poggi C. Calibration of end-debonding strength model for FRP-reinforced masonry. Compos Struct 2015;120:366–77.
[23] Carrara P, Ferretti D, Freddi F. Debonding behaviour of ancient masonry elements strengthened with CFRP sheets. Compos B 2013;45:800–10.
[24] Yuan H, Teng JG, Seracino R, Wu ZS, Yao J. Full-range behaviour of FRP-to concrete bonded joints. Eng Struct 2004;26:553–65.
[25] Zhang XB, Aljewifi H, Li J. Failure behaviour investigation of continuous yarn reinforced cementitious composites. Constr Build Mater 2013;47:456–64.
[26] Zhang XB, Aljewifi H, Li J. Failure mechanism investigation of continuous fibre reinforced cementitious composite by pull-out behavior analysis. In: 20th European conference on fracture. Procedia materials Science, vol. 3; 2014. P. 1377–82.
[27] Carozzi FG, Poggi C. Mechanical properties and debonding strength of fabric reinforced cementitious matrix (FRCM) systems for masonry strengthening. Compos B 2015;70:215–30.
[28] Peled A, Zaguri E, Marom G. Bonding characteristics of multifilament polymer yarns and cement matrices. Compos A 2007;39. 930-393.
[29] Soranakom C, Mobasher B. Geometrical and mechanical aspects of fabric bonding and pull-out in cement composites. Mater Struct 2009;42:765–77.
[30] Andic-Cakir O, Sarijanat M, Tufekci HB, Demirci C, Erdogan UH. Physical and mechanical properties of randomly oriented coir fiber-cementitious composites. Compos B 2014;61:49–54.
[31] Banholzer B, Brockmann T, Brameshuber W. Material and bonding characteristics for dimensioning and modelling of textile reinforced concrete (TRC) elements. Mater Struct 2006;39:749–63.
[32] Dvorkin D, Poursaee A, Peled A, Weiss WJ. Influence of bundle coating on the tensile behavior, bonding, cracking and fluid transport of fabric cement-based composites. Cement Concr Compos 2013;42:9–19.
[33] Aljewifi H, Fiorio B, Gallias JL. Pull out behaviour of a glass multi-filaments yarn embedded in a cementitious matrix. In: EURO-C 2010. Computational modelling of concrete structure, Schladming, Austria; 2010.